CHEMISTRY

Dynamic structural evolution of iron catalysts involving competitive oxidation and carburization during CO_2 hydrogenation

Jie Zhu[1], Peng Wang[2], Xiaoben Zhang[3], Guanghui Zhang[1]*, Rongtan Li[4], Wenhui Li[1], Thomas P. Senftle[2], Wei Liu[3], Jianyang Wang[1], Yanli Wang[1], Anfeng Zhang[1], Qiang Fu[3,4], Chunshan Song[1,5]*, Xinwen Guo[1]*

Identifying the dynamic structure of heterogeneous catalysts is crucial for the rational design of new ones. In this contribution, the structural evolution of Fe(0) catalysts during CO_2 hydrogenation to hydrocarbons has been investigated by using several (quasi) in situ techniques. Upon initial reduction, Fe species are carburized to Fe_3C and then to Fe_5C_2. The by-product of CO_2 hydrogenation, H_2O, oxidizes the iron carbide to Fe_3O_4. The formation of Fe_3O_4@(Fe_5C_2+Fe_3O_4) core-shell structure was observed at steady state, and the surface composition depends on the balance of oxidation and carburization, where water plays a key role in the oxidation. The performance of CO_2 hydrogenation was also correlated with the dynamic surface structure. Theoretical calculations and controll experiments reveal the interdependence between the phase transition and reactive environment. We also suggest a practical way to tune the competitive reactions to maintain an Fe_5C_2-rich surface for a desired C_{2+} productivity.

INTRODUCTION

The structures of heterogeneous catalysts are usually dynamic during redox reactions such as CO_2 hydrogenation, where reaction-driven phase transformation or surface reconstruction is often observed (*1*–*5*). Recently, iron-based catalysts have emerged as an active and selective alternative for CO_2 hydrogenation into value-added hydrocarbons, and they have been shown to undergo (pre-) reduction, carburization, and oxidation as well (*6*–*9*). Identifying the dynamic structure and understanding the structure-performance relationship during CO_2 hydrogenation are highly desirable for clarification of the reaction mechanism and rational design of new catalysts (*10*–*14*). To date, although much attention has been paid to the steady-state performance and the static structure of the catalysts, the dynamic evolution of the structure and performance have rarely been studied.

Nanoscale metallic iron and iron carbide are easily oxidized with exposure to air, which brings uncertainty to the characterizations. The phase transformation and surface reconstruction of iron carbide occur during CO hydrogenation [Fischer-Tropsch synthesis (FTS)] (*15*, *16*), which possibly also occur during CO_2 hydrogenation, given that the two reactions share similar conditions. The observation on spent catalysts is more likely a reflection of an accumulated result over time on stream (TOS), unless time-resolved characterizations are used. Moreover, because of the limitation of characterization techniques, it is still hard to distinguish the diverse iron species ($Fe/FeO_x/FeC_x$) and characterize the surface structure, which is of more significance for catalysis.

The structural evolution of iron-based catalysts has been investigated more widely in FTS (*17*–*20*). By using in situ x-ray diffraction (XRD) and Raman, Paalanen *et al.* (*18*, *19*) monitored the evolution of α-$Fe/FeO_x/FeC_x$ phases during FTS, where the addition of Na and S promotes the reduction of Fe_3O_4 to iron carbides. Wang *et al.* (*20*) found the formation of core-shell structures under long-term FTS conditions over various iron catalysts (Fe_2O_3, χ-Fe_5C_2, θ-Fe_3C, and α-Fe). In addition, note that carburization is affected by the complex surface microenvironment, where the competitive oxygen removal, carbon permeation, hydrogenation, and carbon deposition reactions occur. By interfering them, Tang *et al.* (*21*) yielded high-purity Fe_5C_2 as an effective FTS catalyst.

The stronger oxidation capability of CO_2 compared with CO makes the structural evolution more complicated in CO_2 hydrogenation. In general, Fe_3O_4 and Fe_5C_2 are the main phases on spent catalysts (*22*, *23*). Skrypnik *et al.* (*24*) investigated the steady-state composition of $Fe_xO_yC_z$ catalysts (mixture of α-Fe, iron carbides, and oxides) along the catalyst bed, which suggests that Fe_3O_4, FeO, and Fe are converted into iron carbides under reaction conditions. Zhao *et al.* (*25*) developed an Fe_2N@C catalyst for selective CO_2 hydrogenation to hydrocarbons and found that iron nitrides are in situ converted to highly active iron carbides. Similarly, Zhang *et al.* (*26*) tracked the transformation of the mixture of Fe and Fe_3O_4 by using in situ XRD and Raman and observed the carburization of α-Fe to χ-Fe_5C_2 and γ-Fe to θ-Fe_3C. Besides carburization, they also showed that the CO-activated Fe_5C_2 is oxidized to Fe_3O_4 in CO_2 hydrogenation (*27*). Such a transformation strongly depends on the precursors of the catalysts, their microstructure, reaction, and treatment conditions (*20*, *24*, *28*). After the pre-reduction, Fe(0) is commonly used for CO_2 hydrogenation and the performance changes with TOS (*29*, *30*). However, detailed experimental observations and in-depth understandings on the progressive structural evolution of Fe(0) are still lacking. Likewise, questions concerning the driving force of the structural evolution, the stability of catalysts, and dynamic structure-performance relationship remain to be established.

[1]State Key Laboratory of Fine Chemicals, PSU-DUT Joint Center for Energy Research, School of Chemical Engineering, Dalian University of Technology, Dalian 116024, China. [2]Department of Chemical and Biomolecular Engineering, Rice University, Houston, TX 77005, USA. [3]Dalian National Laboratory for Clean Energy, Dalian Institute of Chemical Physics, Chinese Academy of Sciences, Dalian 116023, China. [4]State Key Laboratory of Catalysis, Dalian Institute of Chemical Physics, Chinese Academy of Sciences, Dalian 116023, China. [5]Department of Chemistry, Faculty of Science, The Chinese University of Hong Kong, Shatin, NT, Hong Kong, China.
*Corresponding author. Email: gzhang@dlut.edu.cn (G.Z.); chunshansong@cuhk.edu.hk (C.S.); guoxw@dlut.edu.cn (X.G.)

Here, we prepared Fe(0) nanoparticles (NPs) and tracked the bulk and surface structure with TOS in CO_2 hydrogenation. Multiple (quasi) in situ structural characterizations were carried out on the spent catalysts without exposure to air, including in situ XRD, quasi–in situ x-ray photoelectron spectroscopy (XPS), Mössbauer spectroscopy, and high-resolution transmission electron microscopy (HRTEM). Meanwhile, by analyzing the activity and selectivity over pure-phase model catalysts (Fe_3O_4, Fe_3C, and Fe_5C_2), we inferred the atomic-level surface structural changes. Theoretic calculations and controlled experiments were carried out to further explore the intrinsic driving force of the structural evolution. Moreover, we suggest a practical way to regulate the transformation of the active iron species and the catalytic performance.

RESULTS AND DISCUSSION

Catalytic performance

The monodispersed and crystalline Fe(0) catalysts can be prepared by the pre-reduction of Fe_2O_3 precursor (figs. S1 and S2). The diffusion limitation has been ruled out (fig. S3); the catalytic performance at 320°C is shown in Fig. 1A and table S1. The data of catalytic performance can be divided into three stages with a linear fitting for each stage (fig. S4). Stage I is an induction period. In the first 2 hours of TOS, a rapid increase of CO_2 conversion from 18 to 39% and C_{2+} selectivity from 20 to 57% and decrease of CH_4 selectivity from 56 to 35% and CO selectivity from 24 to 7% were observed. From the second to the 15th hour, the conversion gradually decreases to 28%, and the selectivity to C_{2+} hydrocarbons decreases to 46%; this deactivation period is termed as stage II. According to the slope of the linearly fitted line in fig. S4A, the deactivation rate in stage II is 0.48%/hour. We defined stage III as the steady state with deactivation rate lower than 0.05%/hour. In this stage, the conversion and selectivity remain almost constant at least for the next 20 hours. Similarly, the chain growth factor α calculated from Anderson-Schulz-Flory model increases during the first 2 to 3 hours, followed by a decreasing period and a steady state (Fig. 1C). The highest α is 0.47, and the highest C_{2+} and C_{5+} selectivity (excluding CO) are 61 and 14%, respectively, at the TOS of 3 hours. These three stages can be retarded and more clearly observed at 300°C (Fig. 1B), and both the activation and deactivation rates are lower than that at 320°C (fig. S4B). The induction period is longer (~18 hours) at 280°C, and it takes less time (~7 hours) to go into the steady stage at 340°C (fig. S5). Most previous studies focused on the performance at stage III, usually after 5 to 10 hours on stream, while this work pays more attention to the dynamic stages I and II, that is, the activation and deactivation, where the structures are evolving.

Sintering usually leads to the decreased conversion for less active sites exposed. However, the loss of the surface area of the Fe catalyst mainly occurs during the first 3 hours (Fig. 1D), inconsistent with the increasing CO_2 conversion during this period. The reaction rate normalized by the surface area continuously increases from 0 to 0.57 $mmol_{CO2}\ min^{-1}\ m^{-2}$ during the first 3 hours and then decreases to 0.50 after 10 hours on stream, which further proves that the deactivation should mainly not result from sintering.

Structural characterizations

The iron species in the spent catalysts after 1, 3, 10, and 40 hours on stream at 320°C (denoted as Fe-*x*h, where *x* stands for TOS) were

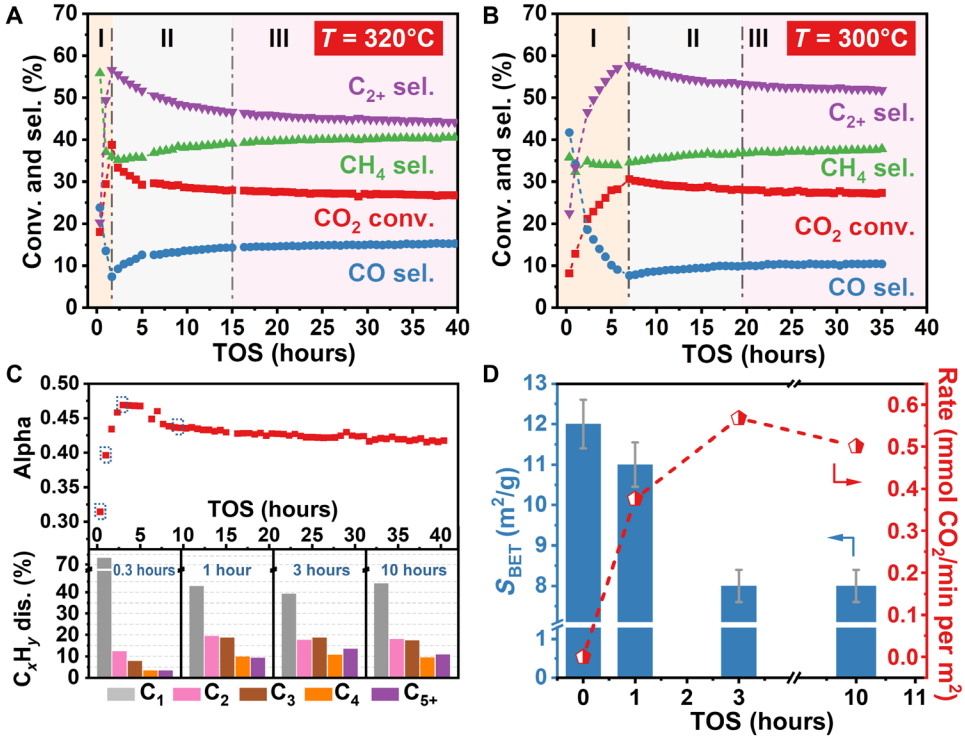

Fig. 1. CO_2 hydrogenation performance versus TOS. Conversion and selectivity at (**A**) 320° and (**B**) 300°C. (**C**) Chain growth factor and hydrocarbon distribution at 320°C. (**D**) Specific surface area of spent catalysts and CO_2 conversion rate at 320°C. Reaction conditions: P = 3 MPa, gas hour space velocity (GHSV) = 18,000 ml $hour^{-1}$ g_{cat}^{-1}, and CO_2/H_2 = 1:3.

characterized by the ^{57}Fe Mössbauer spectroscopy, and the results are shown in fig. S6 and table S2. From the quantitative analysis in Fig. 2C, there is 57% α-Fe in Fe-1h, and only 7 and 3% remains in Fe-3h and Fe-10h, respectively. There is 26% FeC_x in Fe-1h, and the content of carbides increases to 31% (11% Fe_3C and 20% Fe_5C_2) in Fe-3h and then marginally changes (34%) in Fe-10h. It indicates that the carburization of Fe mainly occurs during the first hour. However, a delay for oxidation was observed, where Fe_3O_4 presents with a fraction of 6% in Fe-1h and 61% in Fe-3h. Meanwhile, there is 11% Fe_2O_3 besides 52% Fe_3O_4 in Fe-10h, and Fe-40h contains mainly 20% Fe_5C_2 and 80% Fe_3O_4.

From the XRD patterns in Fig. 2 (A and B), only metallic Fe was observed in the reduced catalyst. The diffractions of Fe_3O_4 can be clearly observed in Fe-3h and are more intense in Fe-10h and Fe-40h. The quantitative analysis (Fig. 2C and table S3) shows that there is 83% α-Fe in Fe-1h, and the content of carbide (10%) is lower than that given by Mössbauer (27%). This might be due to the presence of surface amorphous carbides that are not detected by XRD. For Fe-3h, 65% crystalline Fe_3O_4 and 27% FeC_x were observed, consistent with the rapid carburization and oxidation suggested by the Mössbauer spectra. With the reactions going on, more crystalline Fe_3O_4 (75%) was produced at the TOS of 10 hours, and the crystalline compositions remain almost unchanged during stage III, where 78% Fe_3O_4 and 22% Fe_5C_2 were observed for Fe-40h, consistent with the Mössbauer results.

It has been shown that Fe or FeC_x could be oxidized in CO_2 hydrogenation (*31*). Liang *et al.* (*32*) found more than 90% Fe_3O_4 on the unpromoted Fe catalyst after 10 hours on stream, and 33% Fe_3O_4 was observed by Wei *et al.* (*33*) with the addition of 0.7% Na. Here, the results show that the surface carburization of Fe NPs takes place first to form amorphous or ill crystalline iron carbide during the first 1 hour. Then, a large amount of iron oxides are formed rapidly in the next 2 hours, accompanied by the further crystallization of iron carbide. Then, the oxidation continues until a balanced composition of iron oxides and carbides is reached.

In addition, in the enlarged XRD region in Fig. 2B, with the increasing TOS, the diffractions at 37.7° and 39.7° disappear; those at 42.9°, 43.6°, and 45.9° (rhombus symbols) become weaker, while the diffractions at 39.4°, 44.2°, 47.3°, and 50.2° (heart-shaped symbols) get more intense; these results suggest that Fe_3C can transform into Fe_5C_2. The carburization process was next tracked by in situ XRD at 320° and 340°C, shown in fig. S7 and Fig. 2 (D to F), respectively. In the heatmap (Fig. 2D), the diffractions of FeC_x appear after 20-min TOS. With the TOS increasing to 250 min, the typical diffractions of Fe_5C_2 at 43.5° and 44.1° gradually become more intense (green to light yellow and then to red). This can also be observed in the in situ XRD patterns in Fig. 2E and signal changes in Fig. 2F. Besides, the diffractions at 47.3° and 50.0° become stronger; those at 35.2°, 37.5°, and 39.6° shift to lower angles. The results convincingly indicate that metallic Fe can transform into FeC_x within a short time (20 min)

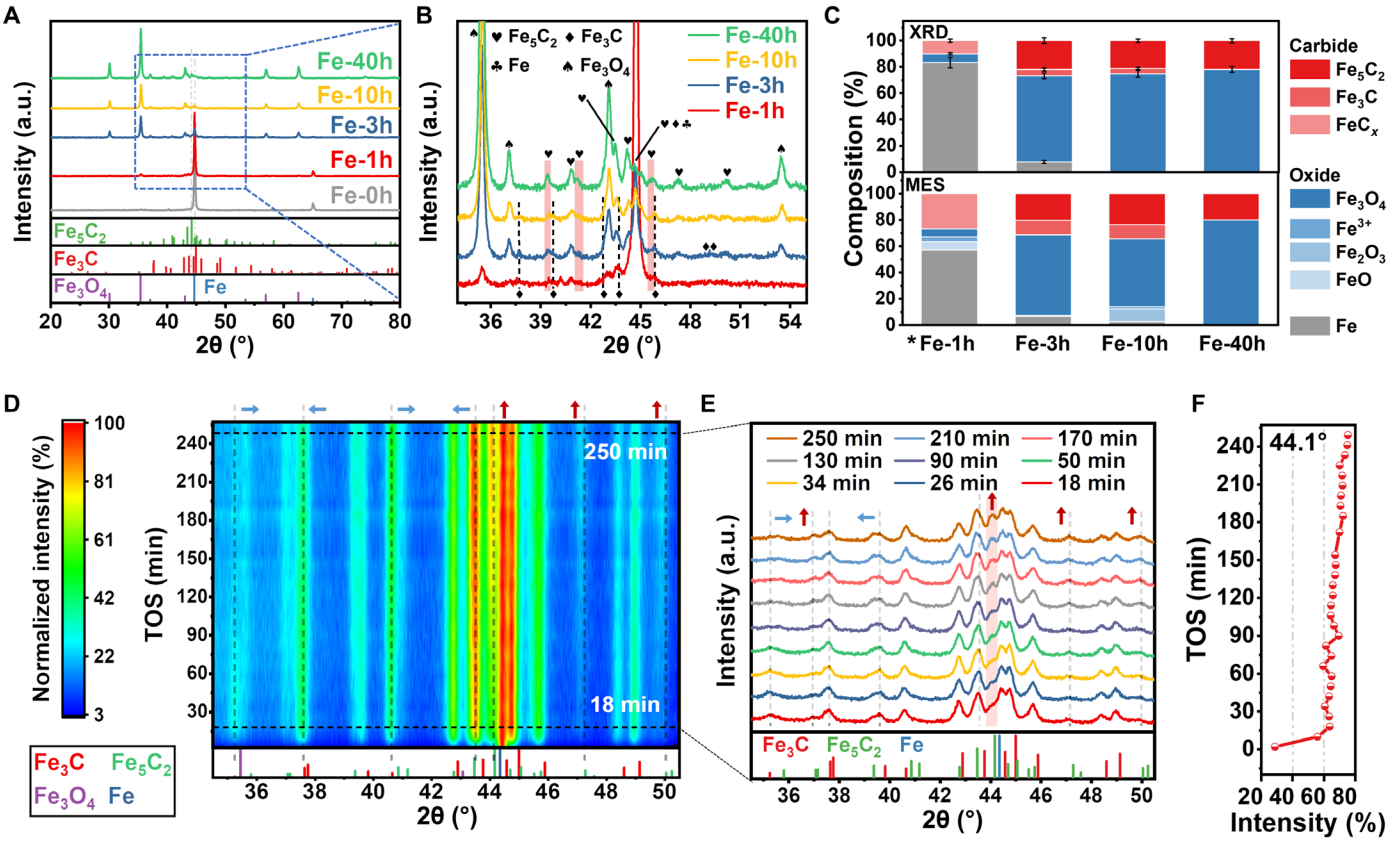

Fig. 2. Analysis of the bulk composition of spent catalysts. (**A**) Overview and (**B**) the enlarged regions of XRD patterns. (**C**) Quantitative results of XRD and Mössbauer (MES) characterizations. *The low-content and indistinguishable Fe_3C and Fe_5C_2 in Fe-1h are collectively noted as FeC_x. (**D**) Heatmap and (**E**) in situ XRD patterns for Fe(0) during CO_2 hydrogenation. Test conditions: $T = 340$°C, $P = 0.8$ MPa, and $CO_2/H_2 = 1{:}3$. (**F**) The intensity change of diffraction peak of Fe_5C_2 at 44.1° in (D). The standard powder diffraction file cards are Fe (87-0721), Fe_3C (65-2413), Fe_5C_2 (89-7272), and Fe_3O_4 (89-3854). a.u., arbitrary units.

from the onset of CO_2 hydrogenation, and the carbon-deficient Fe_3C can transform into carbon-rich Fe_5C_2, which is thermodynamically more stable under these conditions according to carbon potential theory (*34*). Fe_3C has been observed to evolve into Fe_5C_2 under typical FTS conditions (~300°C) (*35*), but it was not yet established in CO_2 hydrogenation.

Carbonaceous species were also determined by temperature-programmed hydrogenation (TPH) tests, and the deconvoluted profiles are shown in Fig. 3A. For Fe-1h, a peak of CH_4 signal locates at a relatively low temperature of 328°C and a main peak locates at 348°C, corresponding to the hydrogenation of atomic carbon and polymethylene, respectively (*36*, *37*). There is also a small shoulder peak at 382°C ascribed to surface or amorphous carbide, which is consistent with its weak diffraction. For Fe-3h and Fe-10h, a small shoulder peak of amorphous carbide at 382°C was observed, but the main peaks locate at 407° to 428°C, corresponding to the crystalline carbide (*26*). The largest peak for Fe-10h locates at 428°C, 4°C higher than that for Fe-3h. The ratio of surface to crystalline carbide calculated from the peak area (table S4) for Fe-10h is 0.12, lower than that for Fe-3h (0.28), suggesting the increased crystallinity of FeC_x.

In addition, the main peak at 261°C for Fe-1h at the mass signal of H_2O corresponds to surface iron oxides (fig. S8). The main peak for Fe-3h and Fe-10h locating at 395°C is ascribed to bulk crystalline Fe_3O_4, consistent with the XRD and Mössbauer results. Meanwhile, 257-nm ultraviolet (UV) Raman was used to verify the surface (ca. 5 to 10 nm) structure (Fig. 3B). For all the 1-, 3-, and 10-hour spent catalysts, a Raman band at 670 cm^{-1} and a broad band at 1500 to 1700 cm^{-1} are observed, which are ascribed to A_{1g} band of Fe_3O_4 and carbonaceous species, respectively (*38*, *39*).

The morphological information of the spent catalysts is provided by HRTEM images (Fig. 4). For Fe-1h, an amorphous layer can be observed, and the inner material is confirmed as α-Fe on the basis of the lattice spacing of 1.99 Å, showing a core-shell structure (Fig. 4E). The electron energy loss spectra (EELS) elemental distribution (Fig. 5, A and D) shows that there are both carbon and oxygen on the surface for Fe-1h, and there is almost only Fe observed in the inner part. The TPH, XRD, and Mössbauer results suggest the formation of surface amorphous iron oxide and iron carbide, and the mapping image gives a direct view of the Fe@FeC_xO_y structure. The core-shell structure can be more clearly observed for the other samples. For Fe-3h, the core is mainly Fe_3O_4 and there are nanocrystals of both Fe_5C_2 and Fe_3O_4 on the surface (Fig. 4F), and the EELS mapping shows that the carbon distributes on the surface, while the oxygen signals appear at the inner region (Fig. 5E). The core-shell structures of Fe-10h and Fe-40h are similar, where the inner Fe_3O_4 appears highly crystalline with ordered lattice (Fig. 4, G and H). The Fe_3O_4 core and the (Fe_3O_4+Fe_5C_2) shell are also identified by EELS spectra (Fig. 5F and fig. S9). The thickness of the mixture shell is 8 to 12 nm (fig. S10). The mapping images and the formed crystalline Fe_3O_4 core show that oxygen migrates from the surface to the bulk, while iron carbides are only formed on the surface (Fig. 5G).

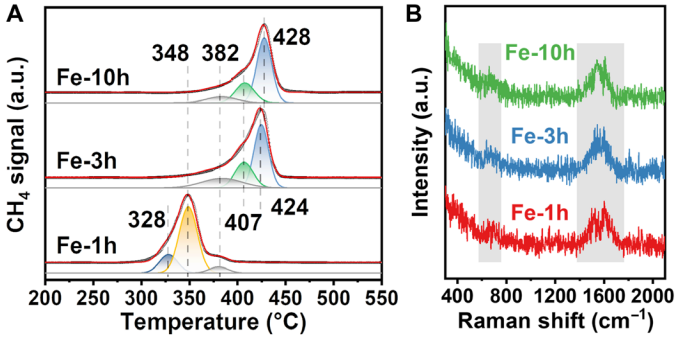

Fig. 3. Characterizations on carbon and iron species. (**A**) TPH profiles with the mass signal of CH_4 and (**B**) UV Raman spectra of spent catalysts using 257-nm radiation.

Note that there is no remarkable difference on the bulk structure between Fe-3h and Fe-10h, although they have distinct catalytic performances. To investigate the chemical state of the surface iron species, the binding energy of Fe core-level electron was measured by quasi–in situ XPS. In Fig. 6A, a peak at 706.5 eV of Fe-1h is assigned to the $2p_{3/2}$ peak of metallic Fe (*31*). It shifts to 707 to 708 eV for Fe-3h, indicating the carburization of Fe(0) to iron carbide (*40*, *41*). This can be verified by the C 1s spectra in fig. S11, where a shoulder peak at 283.5 eV assigned to iron carbide (*42*) appears for Fe-3h. For Fe-10h, the peak at ~707 eV becomes smaller while the peak at ~710 eV assigned to FeO_x grows (*40*, *42*), suggesting the oxidation of surface iron species. In addition, the FeO_x peak shifts from 710.1 to 710.6 eV along with TOS, corresponding to the increasing oxidation degree. The quantitative analysis is based on the deconvolution of Fe 2p XPS spectra, shown in Fig. 6 (B to D) and table S5. For Fe-1h, besides the $2p_{3/2}$ peak at 706.5 eV assigned to Fe(0), signals of Fe_5C_2 at 707.0 eV, Fe_3C at 708.0 eV, and FeO_x at 709.8 and 711.4 eV were also observed (*40*–*42*). The XPS results suggest that both surface carburization and oxidation occur during the first 1 hour on stream. The peak of Fe(0) can hardly be observed on Fe-3h, and the content of Fe_5C_2 increases from 8.4 to 20.9% (table S5). In addition, that of Fe_3C decreases from 13.2 to 8.0%, indicating the continuous carburization of Fe from carbon-deficient Fe_3C to carbon-rich Fe_5C_2 during 1 to 3 hours. For Fe-10h, the ratio of Fe(C_x) to FeO_x decreases from ~40 to 13%, corresponding to the surface oxidation in this period.

Surface structure

Even so, characterizing the (e.g., sub–2 nm) surface of Fe catalyst is challenging, especially when diverse iron species exist. The catalytic performance can be a sensitive probe for analyzing the surface composition. For this purpose, the relation between iron species and catalytic performance was established on the pure model catalysts—Fe_3O_4, Fe_3C, and Fe_5C_2—after the diffusion limitation has been ruled out (fig. S12). Under identical conditions (Fig. 7A), CO_2 conversion rate (normalized by the surface area) on Fe_5C_2 is 5.36 mmol $hour^{-1}$ m^{-2}, higher than that on Fe_3C (1.91 mmol $hour^{-1}$ m^{-2}) and 10 times higher than that on Fe_3O_4 (0.51 mmol $hour^{-1}$ m^{-2}). The conversion rate over FeC_x is more than 20 times higher than that on Fe_3O_4 at a similar conversion level (table S6). The product distribution at different CO_2 conversion over Fe_3C is similar to Fe_5C_2 (tables S6 and S7), which can catalyze the production of C_{2+} hydrocarbons either directly from CO_2 or going through CO intermediate (*26*, *43*, *44*). Conversely, CO is the major product (more than 70%) on Fe_3O_4. The C_{2+} formation rate over Fe_5C_2 and Fe_3C are 2.14 and 0.73 mmol $hour^{-1}$ m^{-2}, respectively, 30 to 100 times higher than that on Fe_3O_4. That is, the ability to catalyze C_{2+} production ranks as Fe_5C_2 > Fe_3C >> Fe_3O_4. Density functional theory (DFT) investigations showed that CO_2 activation is more facile on Fe_5C_2 and Fe_3C than on Fe_3O_4 (*45*, *46*), and Han and colleagues (*27*, *39*) found that the transition of Fe_5C_2 to Fe_3O_4 causes the deactivation in CO_2 hydrogenation.

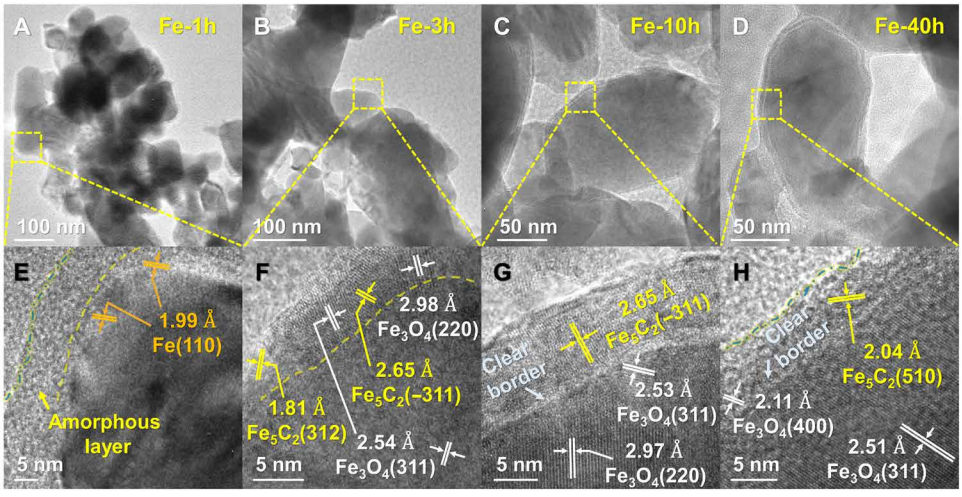

Fig. 4. HRTEM images of the spent catalysts. (**A** and **E**) Fe-1h, (**B** and **F**) Fe-3h, (**C** and **G**) Fe-10h, and (**D** and **H**) Fe-40h.

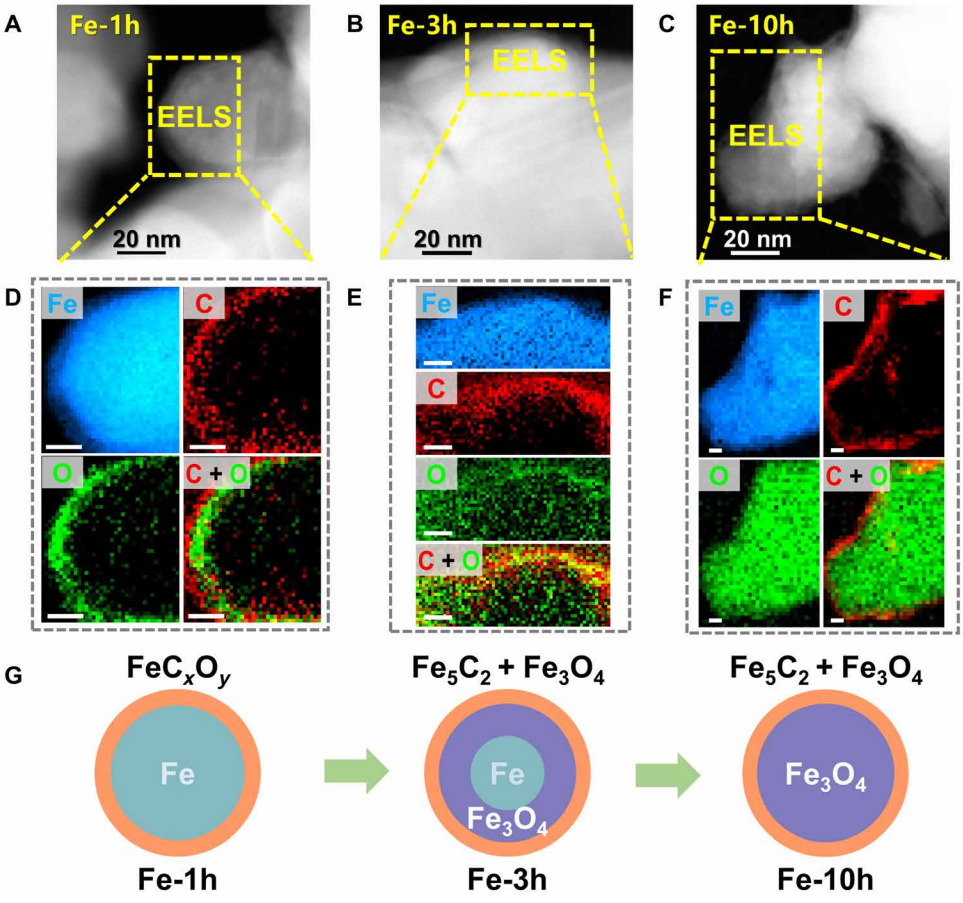

Fig. 5. Microstructure of Fe-xh catalysts. High-angle annular dark-field–scanning transmission electron microscopy (HAADF-STEM) images of (**A**) Fe-1h, (**B**) Fe-3h, and (**C**) Fe-10h. EELS elemental distribution of (**D**) Fe-1h, (**E**) Fe-3h, and (**F**) Fe-10h. Scale bars, 10 nm. (**G**) Schematic diagrams of the evolved microstructure. FeC_xO_y represents the amorphous and coexisted iron oxide and carbide.

From the comparison on the performance over model catalysts and Fe NPs with different TOS (Fig. 7B), Fe-1.7h exhibits a CO_2 conversion (~38%) and product distribution similar to pure Fe_5C_2 under the same conditions, indicating that it has an Fe_5C_2-rich surface. With the limited contribution of Fe_3O_4 as mentioned, the decreased CO_2 conversion (~28%) over Fe-10h should be attributed to the loss of Fe_5C_2 sites. This is verified by the similar product distribution on Fe-10h to that on pure Fe_5C_2 at a conversion of 28% [gas hour space

velocity (GHSV) increasing from 18,000 to 72,000 ml hour^{-1} g_{cat}^{-1}]. On the basis of the quantitative analysis by quasi–in situ XPS (Fig. 6 and table S5), the content of iron carbide is highest on Fe-3h and it also exhibits the highest CO_2 conversion compared with Fe-1h and Fe-10h (fig. S13). The content of Fe_5C_2 correlates well with C_{2+} formation rate, which proves that Fe_5C_2 is the main active species for C_{2+} production. Combing the characterization and catalytic performance, we can conclude that the low conversion on Fe-1h results from fewer FeC_x sites, and the improved C_{2+} production on Fe-1.7h is caused by the further carburization and the transformation of surface Fe_3C to Fe_5C_2. The deactivation in stage II is due to the surface oxidation of iron carbides.

Consequently, we can conclude the evolution of surface and bulk structure of Fe(0) catalyst (Fig. 8A). First, the dissociated carbon species react with the surface of Fe NPs to form an amorphous layer of iron carbides during the first 1 hour on steam. As the reactions get started, iron oxides were also formed. The oxygen can migrate into the subsurface, while carbon mainly carburizes the surface layers (Fe to Fe_3C then to the carbon-rich Fe_5C_2) during TOS of 2 to 3 hours. This Fe_5C_2-rich surface gives the highest CO_2 conversion rate, C_{2+} selectivity, and chain growth factor. Once the crystalline Fe_3O_4 core is formed, excess oxygen will oxidize the surface iron (carbide), leading to deactivation. Last, the surface oxidation, H_2 reduction, and carburization reach a dynamic balance, leading to a stable Fe_3O_4@(Fe_5C_2+Fe_3O_4) core-shell structure and a steady catalytic performance.

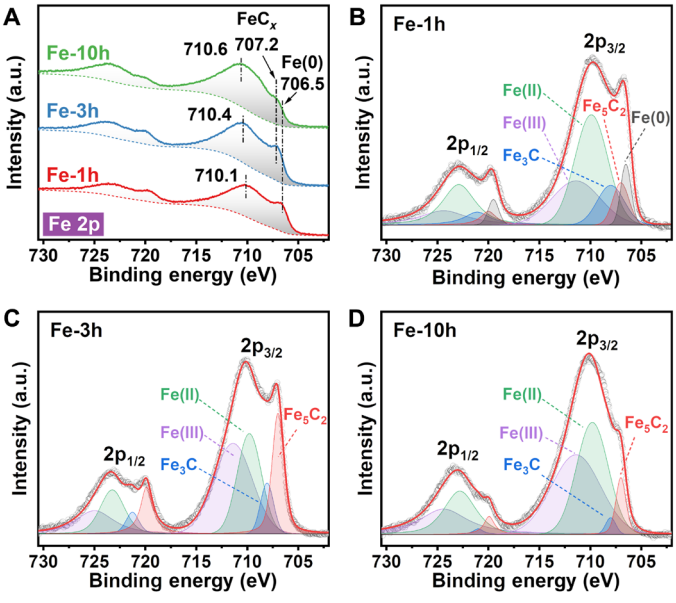

Fig. 6. Quasi–in situ XPS spectra of Fe-xh catalysts. (**A**) Fe 2p spectra. Deconvoluted spectra of (**B**) Fe-1h, (**C**) Fe-3h, and (**D**) Fe-10h.

Driving force of the structural evolution

To understand the evolution of Fe NPs, we applied DFT and ab initio thermodynamics (*47*). Perdew-Burke-Ernzerhof (PBE)+U (*48*, *49*) calculations were performed to construct the phase diagram to locate the state of the system at reaction conditions. The bulk energy of Fe, Fe_5C_2, Fe_3C, FeO, Fe_3O_4, and Fe_2O_3 were computed, where a U correction was applied for oxides to account for the localized d state electrons with a value of 4 eV (*50*). To make the energies from generalized gradient approximation (GGA) (metal and carbides) and PBE+U (oxides) comparable, we derived a correction term (ΔE_M) to account for the arbitrary reference shift caused by the U correction. We derived a ΔE_M value of 1.67 eV using the formalism described by Li *et al.* (*51*) and Xu *et al.* (*52*). The details for the derivation of ΔE_M are included in table S9. The computed phase diagram for Fe species as a function of chemical potential of carbon (μ_C) and oxygen (μ_O) is shown in Fig. 8B. The calculated free energies of reactants (CO_2/H_2/N_2 = 21:63:16) is located at the red dot in the figure, which falls in the Fe_5C_2 domain. When metallic Fe is exposed to the reactants, there is a substantial thermodynamic driving force leading to a phase transition from Fe to Fe_3C and then to Fe_5C_2, which agrees well with the experimental observations at 0 to 1 hour. However, once the active Fe_5C_2 is formed on the surface, hydrogenation of CO_2 is promoted, releasing oxygen into the gas phase (mostly in the form of H_2O) and leading to the increase of μ_O, which, in turn, causes oxidation of the catalyst. Carburization is more difficult for Fe_3O_4 than for Fe (*24*, *53*), which is evident in the in situ XRD data (fig. S14B), and once oxidation begins, it is more difficult for carbon to permeate and carburize the Fe_3O_4 interlayer. The increase in μ_C also causes a drop of μ_O. Thus, the formation of surface Fe_5C_2 leads to a shift in the reactive environment, as shown by the red-blue arrow in Fig. 8B. The product gas at equilibrium (TOS = 10 hours; compositions are in table S10) is located at the blue dot in

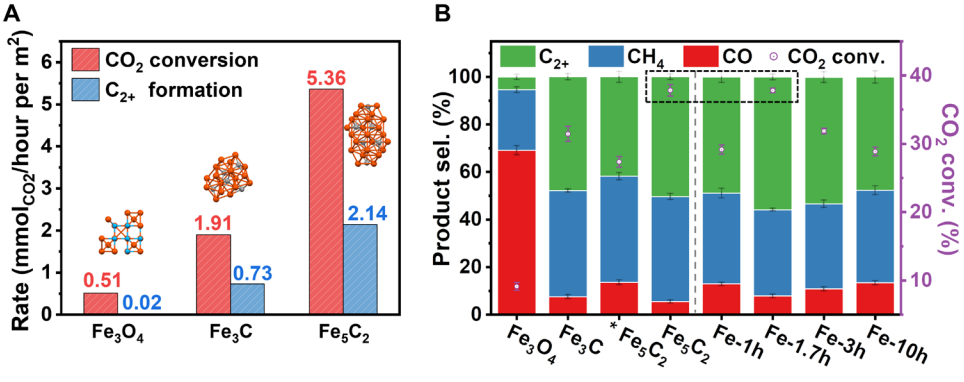

Fig. 7. Comparison of CO_2 hydrogenation performance. (**A**) CO_2 conversion rate and C_{2+} formation rate over different model catalysts. Reaction conditions: P = 3 MPa, T = 320°C, CO_2/H_2 = 1:3, TOS = 20 min, and GHSV = 72,000 ml hour^{-1} g_{cat}^{-1}. (**B**) Product selectivity and CO_2 conversion over model catalysts (on the left of the dashed line) and real Fe(0) catalysts with different TOS (on the right); GHSV = 18,000 ml hour^{-1} g_{cat}^{-1}. *GHSV = 72,000 ml hour^{-1} g_{cat}^{-1}.

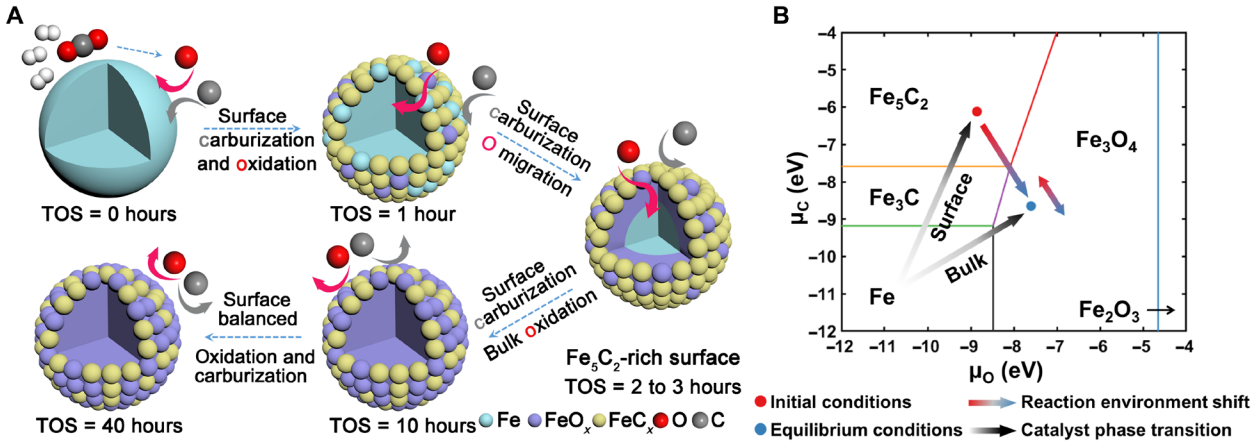

Fig. 8. Analysis of the structural evolution of Fe(0). (**A**) Schematic diagram of the evolution of iron species during CO_2 hydrogenation. The red and gray spheres represent the oxygenous and carbonous species, respectively. (**B**) The computed phase diagram of iron, iron carbides, and oxides. Each solid line is the boundary between two domains, where two species are in equilibrium. The species with the lowest free energy is marked for each domain. The free energies of reactants and equilibrated conditions are calculated on the basis of the compositions shown in table S10. The red-blue arrow is the reactive environment shift. The black arrows are the phase transition of the catalyst.

the Fe_3O_4 domain. As a result, the catalyst loses the thermodynamic driving force for further carburization and the bulk transforms to Fe_3O_4, which corresponds to the 1- to 10-hour segment in Fig. 8A.

The final core-shell structure of the catalyst is the result of the interdependence between the phase formation on the catalyst and the reaction conditions. The formed FeC_x species are active for the CO_2 hydrogenation, which results in higher μ_O and lower μ_C and shifts the reaction conditions toward the Fe_3O_4 domain on the phase diagram. The changed microenvironment, in turn, leads to oxide formation and prohibits carburization. Thus, the formation of carbides exhibits a negative feedback loop, as underscored with a bidirectional arrow in Fig. 8B. If the microenvironment shifts to the red side slightly, then more carbide will be formed on the surface, which promotes oxygen release and pushes the reaction condition back to the equilibrium position and vice versa. The equilibrium reaction condition is located in the Fe_3O_4 domain on the phase diagram, so the core bulk structure of the catalyst will be Fe_3O_4 after a long reaction time. However, full oxidation of the catalyst causes deactivation for CO_2 reduction. In such a case, the reaction conditions would correspond to those of the initial reaction conditions with high μ_C and low μ_O, which will promote the surface carburization. As a result, the catalyst lastly transforms into the core-shell structure with bulk Fe_3O_4 and surface FeC_x.

It can be seen that the oxidation occurs after CO_2 hydrogenation starts. To further explore this dynamic process, we carried out several control experiments. After stage I (induction), the catalyst was treated with 20% CO_2 for 3 hours. When the feed gas was switched back to the mixture of CO_2 and H_2, a decreased CO_2 conversion of 26% and C_{2+} selectivity of 42% were observed (Fig. 9A). In addition, the catalyst was treated with 10% water vapor, similar to its partial pressure under reactions (6 to 12% at a CO_2 conversion of 30%). As a result, CO_2 conversion decreased markedly from 37 to 7%, and CO selectivity increased from 12 to 51% (Fig. 9B). These results reveal that the by-product water notably oxidizes the activated catalyst to form an Fe_3O_4-rich surface. The temperature-programmed oxidation–mass spectrometry (TPO-MS) experiments show that both CO_2 and H_2O can oxidize Fe(0) or FeC_x (fig. S15). The H_2O-TPO profile exhibits an oxidation peak at a lower temperature (416°C) compared to the CO_2-TPO profile (548°C), suggesting that the oxidation by H_2O occurs more easily. After the treatment by CO_2 or H_2O, the catalytic performance recovered gradually, where CO_2 conversion and C_{2+} selectivity increased. This "self-regeneration" verified again that the surface composition and the catalytic performance are determined by the dynamic balance of oxidation and carburization.

In addition, we co-fed water vapor in CO_2 hydrogenation, and the performance also shows three stages (Fig. 9, C and D, and fig. S16). However, with the increased concentration of H_2O from 1 to 10%, lower CO_2 conversion, C_{2+} selectivity, and higher CO selectivity were observed at the steady state. We estimated the gas components at each condition, as shown in table S10. Note that the partial pressure of CO_2 at steady state remains almost unchanged at ~5 bar. However, when we co-fed 10% H_2O, the partial pressure of H_2O is 4.5 bar at steady state (including the H_2O formed during the reaction), only 0.8 bar higher than that without co-feeding H_2O (3.7 bar). The ratio of H_2O in total gas increased from 12% (3.7 bar in 30 bar) to 15% (4.5 bar in 30 bar), while that of CO_2 remains constant at 17%. As a result, this 3% increase of H_2O leads to a much lower CO_2 conversion (~10%), and CO replaces C_{2+} to become the main product. In addition, the quasi–in situ XPS reveals that the surface was almost fully oxidized (fig. S17 and table S11) with co-feeding 5% H_2O. Therefore, H_2O plays a more important role than CO_2 in oxidation during the reaction-induced structural evolution. Moreover, the diffractions of Fe_3O_4 were observed in the in situ XRD patterns in fig. S18, but they disappeared, and the carburization was accelerated in Fig. 2 because of an on-purpose faster removal of H_2O (details in the Supplementary Materials).

After stage III (steady state), the flow rate of reactant gas was decreased from 3600 to 720 ml/hour (Fig. 9G). CO_2 conversion increases from 29 to 34% instantly because of the increased contact time, accompanied by the increased C_{2+} selectivity from 52 to 56%. Nevertheless, the CO_2 conversion continually decreases to 24% in the next 8 hours, even lower than that at the steady state with 3600 ml/hour. Afterwards, the flow rate was set back. However, the CO_2 conversion and C_{2+} selectivity significantly decreased instead

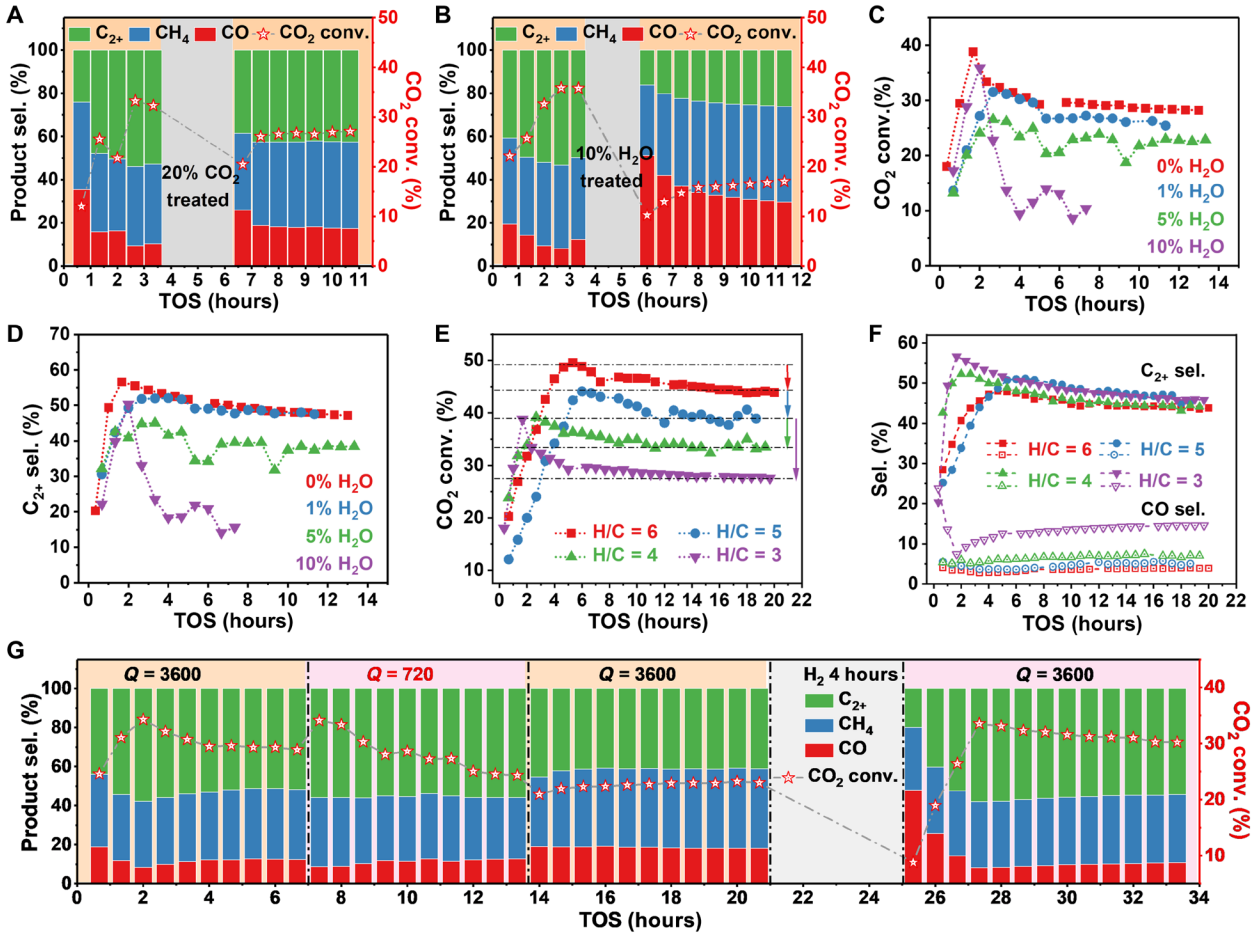

Fig. 9. Dynamic behaviors of CO_2 hydrogenation over Fe catalysts. (**A**) Treating with 20% CO_2 and (**B**) treating with 10% H_2O. (**C**) CO_2 conversion and (**D**) C_{2+} selectivity with co-feeding 1, 5, and 10% H_2O. (**E**) CO_2 conversion. (**F**) CO and C_{2+} selectivity at different H/C. (**G**) Regulating GHSV and treating with H_2. Reaction conditions: P = 3 MPa, T = 320°C, GHSV = 18,000 ml hour^{-1} g_{cat}^{-1} except (G), and H/C = 3 except (E) and (F).

of going back to the original level. The mass transfer limitation is proved to be small (fig. S19), and the dynamic catalytic performance results from the evolution of surface structure. We assumed that more produced water at the high conversion and low GHSV promotes the oxidation, breaking the balance of oxidation and carburization until a new one is established. This indicates that the surface composition is highly sensitive to the microenvironment, which is easily affected by the operating conditions such as GHSV, and we emphasize that more attention should be paid to the real surface structure, especially when these conditions are changed (*54*). With the increasing TOS, the conversion and C_{2+} selectivity increase gradually but are still much lower than the original level within 6 hours. That is, the self-regeneration is too slow, likely because of the slower H_2 dissociation on the FeO_x-rich surface than that on FeC_x, evidenced by H/D exchange experiments (*55*). The following 4-hour H_2 reduction can completely regenerate the catalyst, which confirms that the excessive oxidation by H_2O caused the deactivation.

Therefore, protecting iron carbides from oxidation is an effective way to slow down the deactivation (*24*, *56*). The calculations in Fig. 8B predict that increasing μ_C and decreasing μ_O can promote the carburization. Then, we increased the H/C ratio (feed H_2/CO_2) from 3 to 6 (Fig. 9, E and F, and fig. S20), and the induction period becomes longer under the carbon-deficient atmosphere. The decreased magnitude of CO_2 conversion in stage II becomes lower, and the decrease of C_{2+} selectivity and the increase of CO selectivity could hardly be observed at the H/C ratio of 5 and 6. The deactivation is hindered when more H_2 is fed. The quasi–in situ XPS spectra show that more FeC_x is present with higher H/C ratio (5 versus 3; fig. S17 and table S11), indicating that increasing the partial pressure of H_2 can effectively increase the content of iron carbide and maintain the desired catalytic performance. However, too much hydrogen also causes the termination of chain growth. The deactivation is significantly inhibited, and the highest C_{2+} selectivity of 50% (CO_2 conversion of ~40%) at the steady state is achieved at an optimized H/C ratio of 5. Regulating the ratio of H_2O to H_2 can be a practical strategy to tune the surface competitive carburization and oxidation.

In summary, the structural evolution of Fe(0) catalysts during CO_2 hydrogenation has been investigated. Quasi–in situ analysis on the model catalysts (Fe_3O_4, Fe_3C, and Fe_5C_2) provides a benchmark for correlating the dynamic structure with the catalytic performance. During the induction period, reduced Fe is carburized to Fe_3C and then to Fe_5C_2, which is driven by the thermodynamics. The side product of CO_2 hydrogenation, H_2O, oxidizes the catalysts, resulting in the bulk transition to Fe_3O_4. Theoretical calculations provide

fundamental insight into the interdependence between phase transition and reactive environment, which is the key to the formation of the Fe_3O_4@(Fe_5C_2+Fe_3O_4) core-shell structure. The surface composition depends on the balance of oxidation and carburization, and it is highly sensitive to the operating conditions (e.g., GHSV and H/C), where the by-product water plays a key role. The balance of surface competitive reactions can be tuned by regulating the reaction conditions, providing an opportunity to maintain an Fe_5C_2-rich surface, desired high CO_2 conversion, and C_{2+} selectivity as well. These findings highlight the importance of real-time analysis on the surface structure and the sensitivity of iron (carbide) catalysts to microenvironment during CO_2 hydrogenation to hydrocarbons.

MATERIALS AND METHODS

Preparation of catalysts

Preparation of Fe_2O_3 NPs

Bulk Fe_2O_3 was prepared by a hydrothermal method. Briefly, 2.5 g of $Fe(NO_3)_3{\cdot}9H_2O$ and 1.5 g of urea (analytic grade; Damao Chemical Reagent Factory) were dissolved in 75 ml of deionized water with continuous stirring. The solution was heated to 120°C and kept for 5 hours in a stainless steel Teflon-lined autoclave. Afterwards, the product was centrifuged and washed with deionized water and ethanol three times, dried at 100°C for 12 hours, and then calcined at 500°C in air for 4 hours.

In situ reduction and carburization of Fe_2O_3 NPs

Before the catalytic testing, the as-prepared Fe_2O_3 NPs were reduced or carburized in a fixed-bed reactor. The conditions of the pretreatment were determined on the basis of the in situ XRD results in figs. S2 and S14. Treated with pure H_2 (30 ml min^{-1}) at 3 MPa, Fe_2O_3 can be reduced to Fe_3O_4 at 300°C for 15 min and to metallic Fe at 400°C for 4 hours. Treated with pure CO (30 ml min^{-1}) at ambient pressure, Fe_2O_3 can be carburized to Fe_5C_2 at 350°C for 3 hours and to Fe_3C at 450°C for 30 min.

Catalytic testing

Typically, 0.2 g of the Fe_2O_3 powder catalyst was mixed with quartz sand to 1 ml and then loaded in a quartz tube of 8 mm inner diameter in a continuous-flow fixed-bed reactor. After the pretreatments mentioned above (400°C at 3 MPa in H_2 unless otherwise noted), the reactor was purged with N_2 and set to 320°C. Reactant gas (CO_2/H_2/N_2 = 21:63:16) was then fed in, and the system was pressurized gradually to 3 MPa. The water vapor was co-fed using a steel gas wash bottle, which is placed before the tube reactor and can be pressurized to 3 MPa. The content of water vapor is controlled by regulating the temperature of the bottle based on the saturated vapor pressure. Products were analyzed by an online chromatography (Agilent 7890B), where CO, CH_4, CO_2, and N_2 were detected on a thermal conducted detector and C_2-C_4 hydrocarbons were detected on a flame ionization detector. CO_2 conversion, product selectivity, CO_2 conversion rate, and formation rate of product (normalized by surface area) were calculated using the following equations

$$CO_2\ \text{conversion}\ (\%) = \frac{CO_{2,\text{in}} - CO_{2,\text{out}}}{CO_{2,\text{in}}}$$

$$\text{Selectivity of}\ C_i\ (\%) = \frac{C_{i,\text{out}} \cdot i}{CO_{2,\text{in}} - CO_{2,\text{out}}}$$

$$CO_2\ \text{conversion rate} = \frac{Q_{CO_2} \cdot CO_2\ \text{conversion}}{m_{\text{cat}} \cdot S_{\text{BET}}}$$

$$\text{Formation rate of}\ C_i = CO_2\ \text{conversion rate} \cdot \text{selectivity of}\ C_i$$

where $CO_{2,\text{in}}$ and $CO_{2,\text{out}}$ represent the molar fraction of CO_2 at the inlet and outlet, respectively, $C_{i,\text{out}}$ represents the molar fraction of C_i at the outlet, i represents the number of carbon atoms in C_i; Q_{CO_2} represents the molar flow rate of inlet CO_2, m_{cat} represents the weight of the catalyst used (typically 0.2 g), and S_{BET} represents the specific surface area of the catalyst shown in Fig. 1D and table S8.

The calculation of chain growth factor α is based on the Anderson-Schulz-Flory distribution model, as shown below

$$\ln\frac{W_n}{n} = n \cdot \ln\alpha + \ln\frac{(1-\alpha)^2}{\alpha}$$

where n represents the carbon number of the hydrocarbon products and W_n represents the mass fraction of the product among all hydrocarbons. $\ln(W_n/n)$ is plotted with n, and the slope of the linearly fitted line is lnα (fig. S21).

Catalyst characterization

All the reduced and spent catalysts were transferred along with the tube reactor and stored into a glove box filled with Ar without exposure to air. In addition, most of the preparation or treatments for characterizations were carried out in the glove box. For XRD measurements, the samples were sealed with Kapton tape, and the patterns were acquired on a Rigaku SmartLab 9-kW diffractometer with Cu Kα radiation (λ = 1.5406 Å) at a voltage of 45 kV and a current of 200 mA.

In situ XRD experiments were carried out in an XRK900 reactor chamber (Anton-Paar Corporation) equipped in the diffractometer. The solid powder was pressed into a pellet and then packed into a ceramic sample stage. Typically, pure H_2 or CO was fed at a flow rate of 30 ml min^{-1} for the pretreatment, and the temperature was controlled by a TCU750 temperature control unit. Then, the feed gas was switched to the reactant gas (CO_2/H_2/N_2 = 21:63:16). The XRD sample chamber can be pressurized to 0.8 MPa. The patterns were collected at a speed of 5° min^{-1}, a voltage of 45 kV, and a current of 200 mA using a one-dimensional D/teX detector. The quantitative analysis on XRD data is based on the Reference Intensity Ratio (RIR) method using the PDXL2 software.

For ^{57}Fe Mössbauer measurements, the samples were sealed with film, and the spectra were recorded on a Topologic 500A spectrometer and a proportional counter at room temperature. ^{57}Co (Rh) moving in a constant acceleration mode was used as a radioactive source, and the analysis on spectra was conducted assuming a Lorentzian line shape for computer folding and fitting.

For TPH experiments, the samples were loaded in a U-type tube, sealed with valves, and then taken out from the glove box. About 0.1 g of the sample was loaded and pretreated with N_2 for 1 hour, and then, pure H_2 was fed in. The temperature was then increased to 800°C at a ramp of 5°C/min. CH_4 was monitored using mass signals of 15 (CH_3 fragments of CH_4) instead of 16 to avoid the interference of water vapor and CO_2 cracking (*36*), and H_2O was monitored using mass signals of 18 in a Pfeiffer OmniStar mass spectrometer. For TPO-MS experiments, the sample was treated with 20% CO_2/Ar or ~10%H_2O/Ar. The temperature was then increased to 700°C at a

ramp of 5°C/min. CO and H_2 were monitored using mass signals of 28 and 2, respectively.

UV Raman spectra were recorded using a homemade triple stage UV Raman spectrometer with a spectral resolution of 2 cm^{-1}. UV laser line at 257 nm was from a double-frequency 514-nm laser (model NPL-N-257; Changchun New Industries Optoelectronics Technology Co. Ltd.).

For the quasi–in situ XPS measurements, the sample after reaction was transferred to a glove box through an airtight reaction tube and then transferred to the XPS analysis chamber with a mobile transfer chamber. The sample was kept in reaction atmosphere/inert atmosphere/vacuum during the entire transfer process without exposure to air. The quasi–in situ XPS measurements were carried out on a spectrometer equipped with an Al Kα x-ray source operated at 300 W. Binding energies were calibrated using the C 1s peak at 284.8 eV.

The surface area was determined by N_2 adsorption-desorption on a Quantachrome AUTO-SORB-1-MP sorption analyzer at −196°C and calculated using the Brunauer-Emmett-Teller model. Before the measurements, the samples were degassed at 150°C for 4 hours. The HRTEM images were taken using a FEI Tecnai F30 instrument, and the ethanol suspension of samples was dropped on copper grids for observation.

The high-angle annular dark-field-scanning transmission electron miscroscopy (HAADF-STEM) images and EELS spectrum images were collected on Themis ETEM (Thermo Scientific) located in the Electron Microscopy Center at the Dalian Institute of Chemical Physics, Chinese Academy of Sciences, which was used at 300 kV in dual EELS mode with an energy resolution better than 1.3 eV at a collection angle of 100 mrad. The FeO_xC_y catalysts were loaded onto the Si_3N_4 chip of a microelectromechanical system–based heating holder (Wildfire, DENSsolutions). To rule out the effect of hydrocarbon contamination, the samples were kept at 150° to 200°C in high vacuum ($P < 5 \times 10^{-8}$ mbar).

Computational methods

Computation settings

All DFT computations are performed with the Vienna Ab initio Simulation Package (VASP 5.4.4) (*57*). The PBE functional was used for the exchange-correlation energy (*48*). The projector augmented wave theory was applied to treat frozen core electrons (*58*). The valence electrons of each element type were taken as Fe ($4s^2 3d^6$), C ($2s^2 2p^2$), and O ($2s^2 2p^4$). All calculations were spin-polarized. The plane wave basis was truncated at 500 eV for gas molecules. For optimization of bulk structures, a 650-eV cutoff was applied to mitigate the effect from Pulay stress. Gaussian smearing with 0.05-eV width was applied to oxides and all molecules. First-order Methfessel-Paxton smearing was applied to Fe and carbides (*59*). Brillouin zones were treated with a Monkhorst-Pack *k*-point mesh (*60*). The *k*-points, geometries, and lattice parameters for each bulk structure are summarized in table S12. The energies of all gas molecules are calculated in a cell of 13 Å by 14 Å by 15 Å with a 1 × 1 × 1 *k*-point mesh. The DFT-D3 method for van der Waals interactions was applied for all calculations (*61*). A *U* correction was applied to the calculation of oxides to account for the localized d states (*49*).

Ab initio thermodynamics

Ab initio thermodynamics was applied to construct the bulk phase diagram and locate certain reaction conditions. The formation energy was defined as follows

$$\Delta E_{\text{form}} = E_{\text{Fe}_x\text{O}_y\text{C}_z} - x \cdot E_{\text{Fe}} - y \cdot \mu_{\text{O}} - z \cdot \mu_{\text{C}}$$

where ΔE_{form} is the formation energy; $E_{\text{Fe}_x\text{O}_y\text{C}_z}$ is the DFT energy of a bulk structure with x Fe atoms, y O atoms, and z C atoms; E_{Fe} is the DFT energy of metallic Fe; μ_{O} is the chemical potential of oxygen; and μ_{C} is the chemical potential of carbon. With the assumption of equilibrium between the gas species under reaction conditions, the chemical potential of H, O, and C were derived by free energies of H_2, CO_2, and H_2O, as they are the dominant species present in the gas phase

$$\mu_{\text{H}} = \frac{1}{2} G_{\text{H}_2}$$

$$\mu_{\text{O}} = G_{\text{H}_2\text{O}} - 2\mu_{\text{H}}$$

$$\mu_{\text{C}} = G_{\text{CO}_2} - 2\mu_{\text{O}}$$

where μ_{H} is the chemical potential of hydrogen, G_{H_2} is the free energy of H_2, $G_{\text{H}_2\text{O}}$ is the free energy of H_2O, and G_{CO_2} is the free energy of CO_2. The free energies of molecules were calculated as

$$G_{\text{gas}} = E_{\text{gas}}^{\text{DFT}} + \text{ZPVE}_{\text{gas}} + \Delta \text{H}_{\text{gas}}^{0\text{K}\rightarrow 593.15\text{K}} - TS_{\text{gas}}^{593.15\text{K}} + RT \cdot \ln \frac{P_{\text{gas}}}{P_{\text{ref}}}$$

where $E_{\text{gas}}^{\text{DFT}}$ is the DFT energy of gas molecule, ZPVE_{gas} is the zero-point vibrational energy of the gas molecule, $\Delta \text{H}_{\text{gas}}^{0\text{K}\rightarrow 593.15\text{K}}$ is the enthalpy change of the gas molecule from 0 to 593.15 K, T is the temperature (593.15 K), $S_{\text{gas}}^{593.15\text{K}}$ is the entropy of the gas molecule at 593.15 K, R is the gas constant, P_{gas} is the partial pressure of the gas, and P_{ref} is the reference pressure (1 bar).

SUPPLEMENTARY MATERIALS

Supplementary material for this article is available at https://science.org/doi/10.1126/sciadv.abm3629

REFERENCES AND NOTES

1. X. Zhang, S. Han, B. Zhu, G. Zhang, X. Li, Y. Gao, Z. Wu, B. Yang, Y. Liu, W. Baaziz, O. Ersen, M. Gu, J. T. Miller, W. Liu, Reversible loss of core-shell structure for Ni-Au bimetallic nanoparticles during CO_2 hydrogenation. *Nat. Catal.* **3**, 411–417 (2020).
2. A. Tsoukalou, P. M. Abdala, D. Stoian, X. Huang, M. G. Willinger, A. Fedorov, C. R. Muller, Structural evolution and dynamics of an In_2O_3 catalyst for CO_2 hydrogenation to methanol: An operando XAS-XRD and in situ TEM study. *J. Am. Chem. Soc.* **141**, 13497–13505 (2019).
3. J. Wang, C.-Y. Liu, T. P. Senftle, J. Zhu, G. Zhang, X. Guo, C. Song, Variation in the In_2O_3 crystal phase alters catalytic performance toward the reverse water gas shift reaction. *ACS Catal.* **10**, 3264–3273 (2020).
4. X. Zhang, G. Zhang, W. Liu, F. Yuan, J. Wang, J. Zhu, X. Jiang, A. Zhang, F. Ding, C. Song, X. Guo, Reaction-driven surface reconstruction of $ZnAl_2O_4$ boosts the methanol selectivity in CO_2 catalytic hydrogenation. *Appl Catal B* **284**, 119700 (2021).
5. M. D. Porosoff, X. Yang, J. A. Boscoboinik, J. G. Chen, Molybdenum carbide as alternative catalysts to precious metals for highly selective reduction of CO_2 to CO. *Angew. Chem. Int. Ed.* **53**, 6705–6709 (2014).
6. Y. Xu, P. Zhai, Y. Deng, J. Xie, X. Liu, S. Wang, D. Ma, Highly selective olefin production from CO_2 hydrogenation on iron catalysts: A subtle synergy between manganese and sodium additives. *Angew. Chem. Int. Ed.* **59**, 21736–21744 (2020).
7. M. K. Khan, P. Butolia, H. Jo, M. Irshad, D. Han, K.-W. Nam, J. Kim, Selective conversion of carbon dioxide into liquid hydrocarbons and long-chain α-olefins over Fe-Amorphous AlO_x bifunctional catalysts. *ACS Catal.* **10**, 10325–10338 (2020).
8. Y. Han, C. Fang, X. Ji, J. Wei, Q. Ge, J. Sun, Interfacing with carbonaceous potassium promoters boosts catalytic CO_2 hydrogenation of iron. *ACS Catal.* **10**, 12098–12108 (2020).
9. P. Gao, L. Zhang, S. Li, Z. Zhou, Y. Sun, Novel heterogeneous catalysts for CO_2 hydrogenation to liquid fuels. *ACS Cent. Sci.* **6**, 1657–1670 (2020).

10. X. Jiang, X. Nie, X. Guo, C. Song, J. G. Chen, Recent advances in carbon dioxide hydrogenation to methanol via heterogeneous catalysis. *Chem. Rev.* **120**, 7984–8034 (2020).
11. J. Wang, G. Zhang, J. Zhu, X. Zhang, F. Ding, A. Zhang, X. Guo, C. Song, CO_2 hydrogenation to methanol over In_2O_3-based catalysts: From mechanism to catalyst development. *ACS Catal.* **11**, 1406–1423 (2021).
12. C. Yang, S. Liu, Y. Wang, J. Song, G. Wang, S. Wang, Z. J. Zhao, R. Mu, J. Gong, The interplay between structure and product selectivity of CO_2 hydrogenation. *Angew. Chem. Int. Ed.* **58**, 11242–11247 (2019).
13. C. Meng, G. Zhao, X.-R. Shi, P. J. Chen, Y. Liu, Y. Lu, Oxygen-deficient metal oxides supported nano-intermetallic $InNi_3C_{0.5}$ toward efficient CO_2 hydrogenation to methanol. *Sci. Adv.* **7**, eabi6012 (2021).
14. S. Dang, B. Qin, Y. Yang, H. Wang, J. Cai, Y. Han, S. Li, P. Gao, Y. Sun, Rationally designed indium oxide catalysts for CO_2 hydrogenation to methanol with high activity and selectivity. *Sci. Adv.* **6**, eaaz2060 (2020).
15. J. Yin, X. Liu, X.-W. Liu, H. Wang, H. Wan, S. Wang, W. Zhang, X. Zhou, B.-T. Teng, Y. Yang, Y.-W. Li, Z. Cao, X.-D. Wen, Theoretical exploration of intrinsic facet-dependent CH_4 and C_2 formation on Fe_5C_2 particle. *Appl Catal B* **278**, 119308 (2020).
16. P. Wang, W. Chen, F.-K. Chiang, A. I. Dugulan, Y. Song, R. Pestman, K. Zhang, J. Yao, B. Feng, P. Miao, W. Xu, E. J. M. Hensen, Synthesis of stable and low-CO_2 selective ε-iron carbide Fischer-Tropsch catalysts. *Sci. Adv.* **4**, eaau2947 (2018).
17. J. Zhang, M. Abbas, J. Chen, The evolution of Fe phases of a fused iron catalyst during reduction and Fischer-Tropsch synthesis. *Cat. Sci. Technol.* **7**, 3626–3636 (2017).
18. P. P. Paalanen, S. H. van Vreeswijk, B. M. Weckhuysen, Combined in situ x-ray powder diffractometry/Raman spectroscopy of iron carbide and carbon species evolution in Fe(–Na–S)/α-Al_2O_3 catalysts during Fischer-Tropsch synthesis. *ACS Catal.* **10**, 9837–9855 (2020).
19. P. P. Paalanen, B. M. Weckhuysen, Carbon pathways, sodium-sulphur promotion and identification of iron carbides in iron-based Fischer-Tropsch synthesis. *ChemCatChem* **12**, 4202–4223 (2020).
20. J. Wang, S. Huang, S. Howard, B. W. Muir, H. Wang, D. F. Kennedy, X. Ma, Elucidating surface and bulk phase transformation in Fischer-Tropsch synthesis catalysts and their influences on catalytic performance. *ACS Catal.* **9**, 7976–7983 (2019).
21. L. Tang, L. He, Y. Wang, B. Chen, W. Xu, X. Duan, A.-H. Lu, Selective fabrication of χ-Fe_5C_2 by interfering surface reactions as a highly efficient and stable Fischer-Tropsch synthesis catalyst. *Appl Catal B* **284**, 119753 (2021).
22. G. Song, M. Li, P. Yan, M. A. Nawaz, D. Liu, High conversion to aromatics via CO_2-FT over a CO-reduced Cu-Fe_2O_3 catalyst integrated with HZSM-5. *ACS Catal.* **10**, 11268–11279 (2020).
23. F. Yuan, G. Zhang, J. Zhu, F. Ding, A. Zhang, C. Song, X. Guo, Boosting light olefin selectivity in CO_2 hydrogenation by adding Co to Fe catalysts within close proximity. *Catal. Today* **371**, 142–149 (2021).
24. A. S. Skrypnik, Q. Yang, A. A. Matvienko, V. Y. Bychkov, Y. P. Tulenin, H. Lund, S. A. Petrov, R. Kraehnert, A. Arinchtein, J. Weiss, A. Brueckner, E. V. Kondratenko, Understanding reaction-induced restructuring of well-defined $Fe_xO_yC_z$ compositions and its effect on CO_2 hydrogenation. *Appl Catal B* **291**, 120121 (2021).
25. B. Zhao, M. Sun, F. Chen, Y. Shi, Y. Yu, X. Li, B. Zhang, Unveiling the activity origin of iron nitride as catalytic material for efficient hydrogenation of CO_2 to C_{2+} hydrocarbons. *Angew. Chem. Int. Ed.* **60**, 4496–4500 (2021).
26. Y. Zhang, D. Fu, X. Liu, Z. Zhang, C. Zhang, B. Shi, J. Xu, Y.-F. Han, Operando spectroscopic study of dynamic structure of iron oxide catalysts during CO_2 hydrogenation. *ChemCatChem* **10**, 1272–1276 (2018).
27. Y. Zhang, C. Cao, C. Zhang, Z. Zhang, X. Liu, Z. Yang, M. Zhu, B. Meng, J. Xu, Y.-F. Han, The study of structure-performance relationship of iron catalyst during a full life cycle for CO_2 hydrogenation. *J. Catal.* **378**, 51–62 (2019).
28. L. Luo, M. Wang, Y. Cui, Z. Chen, J. Wu, Y. Cao, J. Luo, Y. Dai, W. X. Li, J. Bao, J. Zeng, Surface iron species in palladium-iron intermetallic nanocrystals that promote and stabilize CO_2 methanation. *Angew. Chem. Int. Ed.* **59**, 14434–14442 (2020).
29. S.-M. Hwang, S. J. Han, H.-G. Park, H. Lee, K. An, K.-W. Jun, S. K. Kim, Atomically alloyed Fe-Co catalyst derived from a N-coordinated Co single-atom structure for CO_2 hydrogenation. *ACS Catal.* **11**, 2267–2278 (2021).
30. J. Wei, J. Sun, Z. Wen, C. Fang, Q. Ge, H. Xu, New insights into the effect of sodium on Fe_3O_4-based nanocatalysts for CO_2 hydrogenation to light olefins. *Cat. Sci. Technol.* **6**, 4786–4793 (2016).
31. M. Lopez Luna, J. Timoshenko, D. Kordus, C. Rettenmaier, S. W. Chee, A. S. Hoffman, S. R. Bare, S. Shaikhutdinov, B. Roldan Cuenya, Role of the oxide support on the structural and chemical evolution of fe catalysts during the hydrogenation of CO_2. *ACS Catal.* **11**, 6175–6185 (2021).
32. B. Liang, H. Duan, T. Sun, J. Ma, X. Liu, J. Xu, X. Su, Y. Huang, T. Zhang, Effect of Na promoter on Fe-based catalyst for CO_2 hydrogenation to alkenes. *ACS Sustainable Chem. Eng.* **7**, 925–932 (2018).
33. J. Wei, Q. Ge, R. Yao, Z. Wen, C. Fang, L. Guo, H. Xu, J. Sun, Directly converting CO_2 into a gasoline fuel. *Nat. Commun.* **8**, 15174 (2017).
34. E. de Smit, F. Cinquini, A. M. Beale, O. V. Safonova, W. van Beek, P. Sautet, B. M. Weckhuysen, Stability and reactivity of ε-χ-θ iron carbide catalyst phases in Fischer-Tropsch synthesis: Controlling μC. *J. Am. Chem. Soc.* **132**, 14928–14941 (2010).
35. T. Herranz, S. Rojas, F. Perezalonso, M. Ojeda, P. Terreros, J. Fierro, Genesis of iron carbides and their role in the synthesis of hydrocarbons from synthesis gas. *J. Catal.* **243**, 199–211 (2006).
36. J. Xu, C. H. Bartholomew, Temperature-programmed hydrogenation (TPH) and in situ Mössbauer spectroscopy studies of carbonaceous species on silica-supported iron Fischer-Tropsch catalysts. *J. Phys. Chem. B* **109**, 2392–2403 (2005).
37. D. Peña, A. Cognigni, T. Neumayer, W. van Beek, D. S. Jones, M. Quijada, M. Rønning, Identification of carbon species on iron-based catalysts during Fischer-Tropsch synthesis. *Appl. Catal. A* **554**, 10–23 (2018).
38. I. Chamritski, G. Burns, Infrared- and Raman-active phonons of magnetite, maghemite, and hematite: A computer simulation and spectroscopic study. *J. Phys. Chem. B* **109**, 4965–4968 (2005).
39. C. Zhang, C. Cao, Y. Zhang, X. Liu, J. Xu, M. Zhu, W. Tu, Y.-F. Han, Unraveling the role of zinc on bimetallic Fe_5C_2-ZnO catalysts for highly selective carbon dioxide hydrogenation to high carbon α-olefins. *ACS Catal.* **11**, 2121–2133 (2021).
40. M. Amoyal, R. Vidruk-Nehemya, M. V. Landau, M. Herskowitz, Effect of potassium on the active phases of Fe catalysts for carbon dioxide conversion to liquid fuels through hydrogenation. *J. Catal.* **348**, 29–39 (2017).
41. F. Lu, X. Chen, Z. Lei, L. Wen, Y. Zhang, Revealing the activity of different iron carbides for Fischer-Tropsch synthesis. *Appl Catal B* **281**, 119521 (2021).
42. M. Al-Dossary, A. A. Ismail, J. L. G. Fierro, H. Bouzid, S. A. Al-Sayari, Effect of Mn loading onto MnFeO nanocomposites for the CO_2 hydrogenation reaction. *Appl Catal B* **165**, 651–660 (2015).
43. J. Zhu, G. Zhang, W. Li, X. Zhang, F. Ding, C. Song, X. Guo, Deconvolution of the particle size effect on CO_2 hydrogenation over iron-based catalysts. *ACS Catal.* **10**, 7424–7433 (2020).
44. J. Liu, G. Zhang, X. Jiang, J. Wang, C. Song, X. Guo, Insight into the role of Fe_5C_2 in CO_2 catalytic hydrogenation to hydrocarbons. *Catal. Today* **371**, 162–170 (2021).
45. X. Nie, L. Meng, H. Wang, Y. Chen, X. Guo, C. Song, DFT insight into the effect of potassium on the adsorption, activation and dissociation of CO_2 over Fe-based catalysts. *Phys. Chem. Chem. Phys.* **20**, 14694–14707 (2018).
46. X. Liu, C. Cao, P. Tian, M. Zhu, Y. Zhang, J. Xu, Y. Tian, Y.-F. Han, Resolving CO_2 activation and hydrogenation pathways over iron carbides from DFT investigation. *J. CO2 Util.* **38**, 10–15 (2020).
47. K. Reuter, Ab Initio Thermodynamics and First-Principles Microkinetics for Surface Catalysis, in *Operando Research in Heterogeneous Catalysis*, J. Frenken, I. Groot, Eds. (Springer International Publishing, 2017), pp. 151–188.
48. J. P. Perdew, K. Burke, M. Ernzerhof, Generalized gradient approximation made simple. *Phys. Rev. Lett.* **77**, 3865–3868 (1996).
49. S. L. Dudarev, G. A. Botton, S. Y. Savrasov, C. J. Humphreys, A. P. Sutton, Electron-energy-loss spectra and the structural stability of nickel oxide: An LSDA+U study. *Phys. Rev. B* **57**, 1505–1509 (1998).
50. L. Wang, T. Maxisch, G. Ceder, Oxidation energies of transition metal oxides within the GGA+U framework. *Phys. Rev. B* **73**, 195107 (2006).
51. Y. Li, Y.-S. Zheng, Y.-A. Zhu, Z.-J. Sui, X.-G. Zhou, D. Chen, W.-K. Yuan, BEEF-vdW+U method applied to perovskites: Thermodynamic, structural, electronic, and magnetic properties. *J. Phys. Condens. Matter* **31**, 145901 (2019).
52. Z. Xu, Y. V. Joshi, S. Raman, J. R. Kitchin, Accurate electronic and chemical properties of 3d transition metal oxides using a calculated linear response U and a DFT + U(V) method. *J. Chem. Phys.* **142**, 144701 (2015).
53. M. Ding, Y. Yang, B. Wu, Y. Li, T. Wang, L. Ma, Study on reduction and carburization behaviors of iron phases for iron-based Fischer-Tropsch synthesis catalyst. *Appl. Energy* **160**, 982–989 (2015).
54. M. Wolf, N. Fischer, M. Claeys, Water-induced deactivation of cobalt-based Fischer-Tropsch catalysts. *Nat. Catal.* **3**, 962–965 (2020).
55. C. Song, X. Liu, M. Xu, D. Masi, Y. Wang, Y. Deng, M. Zhang, X. Qin, K. Feng, J. Yan, J. Leng, Z. Wang, Y. Xu, B. Yan, S. Jin, D. Xu, Z. Yin, D. Xiao, D. Ma, Photothermal conversion of CO_2 with tunable selectivity using Fe-based catalysts: From oxide to carbide. *ACS Catal.* **10**, 10364–10374 (2020).
56. Y. Xu, X. Li, J. Gao, J. Wang, G. Ma, X. Wen, Y. Yang, Y. Li, M. Ding, A hydrophobic FeMn@Si catalyst increases olefins from syngas by suppressing C1 by-products. *Science* **371**, 610–613 (2021).
57. G. Kresse, J. Furthmüller, Efficiency of ab-initio total energy calculations for metals and semiconductors using a plane-wave basis set. *Comput. Mater. Sci.* **6**, 15–50 (1996).
58. P. E. Blochl, Projector augmented-wave method. *Phys. Rev. B Condens. Matter.* **50**, 17953–17979 (1994).

59. M. Methfessel, A. T. Paxton, High-precision sampling for Brillouin-zone integration in metals. *Phys. Rev. B Condens. Matter.* **40**, 3616–3621 (1989).
60. H. J. Monkhorst, J. D. Pack, Special points for Brillouin-zone integrations. *Phys. Rev. B* **13**, 5188–5192 (1976).
61. S. Grimme, J. Antony, S. Ehrlich, H. Krieg, A consistent and accurate ab initio parametrization of density functional dispersion correction (DFT-D) for the 94 elements H-Pu. *J. Chem. Phys.* **132**, 154104 (2010).
62. M. W. Chase Jr., Journal of Physical and Chemical Reference Data Monographs or Supplements, in *NIST-JANAF Thermochemical Tables, Monograph 9* (American Chemical Society, ed. 4, 1998), vol. 9, pp. 1–1951.

Acknowledgments: We acknowledge the Center for Advanced Mössbauer Spectroscopy, Dalian Institute of Chemical Physics, CAS for providing the Mössbauer measurement and analysis. We also thank Z. Feng of Dalian Institute of Chemical Physics in Raman characterization. J.Z. acknowledges M. Mu from Texas A&M University for discussion. **Funding:** This work was supported by the National Key Research and Development Program of China (2016YFB0600902-4), the National Natural Science Foundation of China (21902019, 22072150, and 22172013), the China Postdoctoral Science Foundation (2020M670755), The Liaoning Revitalization Talents Program (XLYC2008032), Open Sharing Fund for the Large-scale Instruments and Equipment of Dalian University of Technology (DUTKFJJ2021126 and DUTKFJJ2021081), The Fundamental Research Funds for the Central Universities [DUT20RC(5)002], and The American Chemical Society Petroleum Research Fund (PRF no. 59759-DNI6). **Author contributions:** Conceptualization: J.Z., G.Z., T.P.S., W. Liu, C.S., and X.G. Methodology: J.Z., P.W., X.Z., R.L., J.W., Y.W., and A.Z. Investigation: J.Z., P.W., X.Z., R.L., J.W., and Y.W. Visualization: J.Z., W. Li, and P.W. Supervision: G.Z., T.P.S., W. Liu, Q.F., A.Z., C.S., and X.G. Writing (original draft): J.Z., P.W., and G.Z. Writing (review and editing): J.Z., P.W., G.Z., R.L., T.P.S., W. Liu, Q.F., C.S., and X.G. **Competing interests:** The authors declare that they have no competing interests. **Data and materials availability:** All data needed to evaluate the conclusions in the paper are present in the paper and/or the Supplementary Materials.

Submitted 13 September 2021
Accepted 14 December 2021
Published 4 February 2022
10.1126/sciadv.abm3629